SF2A 2008
C. Charbonnel, F. Combes and R. Samadi (eds)

MODELLING THE HIGH ENERGY EMISSION OF PULSARS

Pétri, J.[1, 2]

Abstract. To date, seven gamma-ray pulsars are known, showing pulsed emission up to tens of GeV and associated light-curves with a double-pulse structure. We study this pulsed high-energy emission in the framework of the striped wind model. By numerical integration of the time-dependent emissivity in the current sheets, we compute the phase-dependent spectral variability of the inverse Compton radiation. Several light curves and spectra are presented. Pulses are a direct consequence of relativistic beaming. Our model is able to explain some of the high-energy (10 MeV-10 GeV) spectral features and behavior of several gamma-ray pulsars, like Geminga and Vela.

1 Introduction

The high-energy, pulsed emission from rotating magnetized neutron stars is usually explained in the framework of either the polar cap or the outer gap models. In both of these models, the radiation is produced within the light cylinder.

An alternative site for the production of pulsed radiation has been investigated (Kirk et al. 2002) based on the idea of a striped pulsar wind, originally introduced by Coroniti (1990) and Michel (1994). Emission from the striped wind originates outside the light cylinder and relativistic beaming effects are responsible for the phase coherence of the radiation. It has already been shown that this model can satisfactorily fit the optical polarization data from the Crab pulsar (Pétri & Kirk 2005).

We use an explicit asymptotic solution for the large-scale field structure related to the oblique split monopole (Bogovalov 1999). We calculate the properties of the phase-resolved and spectral variability of the pulsed emission and compare our results with high-energy observations of several gamma-ray pulsars.

2 THE STRIPED WIND MODEL

The model used to compute the high-energy pulse shape and the phase-resolved spectrum arising from the striped wind is briefly presented in this section. The geometrical configuration is as follows. The magnetized neutron star is rotating at an angular speed Ω_* directed along the (Oz)-axis i.e. the rotation axis is $\vec{\Omega}_* = \Omega_* \vec{e}_z$. We use a Cartesian coordinate system with coordinates (x, y, z) and orthonormal basis $(\vec{e}_x, \vec{e}_y, \vec{e}_z)$. The stellar magnetic moment $\vec{m} = m\vec{e}_m$, assumed to be dipolar, makes an angle χ with respect to the rotation axis. This angle is therefore defined by $\cos\chi = \vec{e}_m \cdot \vec{e}_z$. The inclination of the line of sight with respect to the rotational axis, and defined by the unit vector $\vec{n}$, is denoted by ζ, we have $\cos\zeta = \vec{n} \cdot \vec{e}_z$. It lies in the ($Oyz$) plane. Moreover, the wind is expanding radially outwards at a constant velocity V close to the speed of light denoted by c.

Our model involves some geometrical properties related to the magnetic field structure and some dynamical properties related to the emitting particles. Furthermore, in order to compute the light curves and the corresponding spectra, we need to know the emissivity of the wind due to inverse Compton scattering. This is explained in the next paragraphs.

2.1 Magnetic field structure

We adopt a geometrical structure of the wind based on the asymptotic magnetic field solution given by Bogovalov (1999). Outside the light cylinder, the magnetic structure is replaced by two magnetic monopoles with equal and opposite intensity. The current sheet sustaining the magnetic polarity reversal arising in this solution, expressed in spherical coordinates (r, θ, φ) is defined by $r_s(\theta, \varphi, t) = \beta r_L \left[\pm \arccos(-\cot\theta \cot\chi) + c\,t/r_L - \varphi + 2\,l\pi\right]$ where $\beta = V/c$, $r_L = c/\Omega_*$ is the

[1] Centre d'étude des Environnements Terrestre et Planétaires, 10-12 avenue de l'Europe 78140 Vélizy
[2] Laboratoire de Radio-Astronomie, École Normale Supérieure, 24 rue Lhomond 75005 Paris

radius of the light cylinder, t is the time as measured by a distant observer at rest, and l an integer. Because of the ideal MHD assumption, this surface is frozen into the plasma and therefore moves also radially outwards at a constant speed V. Strictly speaking, the current sheets are infinitely thin. However, as was already done in the study of the synchrotron polarization of the pulsed emission (Pétri & Kirk 2005) we release this prescription. Indeed, the current sheet are assumed to have a given thickness, parameterized by the quantity Δ_φ. Moreover, inside the sheets, the particle number density is very high while the magnetic field is weak. In whole space, the magnetic field is purely toroidal and given by

$$B_\varphi = B_{\rm L} \frac{R_{\rm L}}{r} \eta_\varphi \tag{2.1}$$

The strength of the magnetic field at the light-cylinder is denoted by $B_{\rm L}$. In the original work of Bogovalov (1999) , the function η_φ is related to the Heaviside unit step function and can only have two values ± 1, leading to the discontinuity in magnetic field. In order to make the transition more smooth, we redefine the function η_φ by

$$\begin{aligned} \eta_\varphi &= \tanh(\Delta_\varphi \, \psi) \\ \psi &= \cos\theta \, \cos\chi + \sin\theta \, \sin\chi \, \cos\left[\varphi - \Omega_* \, (t - \frac{r}{V})\right] \end{aligned} \tag{2.2}$$

With this expression, the transition layer has a thickness of approximately Δ_φ.

2.2 Particle distribution function

The innermost regions of the pulsar magnetosphere is believed to be a site of high-energy pair production feeding the wind with ultra-relativistic electrons and positrons. For these emitting particles, we adopt an isotropic distribution function in momentum space in the comoving frame of the wind. It is given by a power law in energy, with a sharp low and high-energy cut-off, $\gamma_{\rm min}$ and $\gamma_{\rm max}$ respectively, such that the particle number density at time t and position $\vec{r}$ with energy between γ and $\gamma + d\gamma$ is

$$n_e(\gamma, \vec{r}, t) \, d\gamma = K_e(\vec{r}, t) \, \gamma^{-p} \, d\gamma \tag{2.3}$$

with $\gamma_{\rm min} \leq \gamma \leq \gamma_{\rm max}$ and $K_e(\vec{r}, t)$ is related to the number density of emitting particles in the current sheet. The particular form of the magnetic field in the current sheets, decreasing like a tangent hyperbolic function tanh as given in Eq. (2.1), suggests to use a plasma density profile dictated by the exact solution of the relativistic Harris current sheet, namely a secant cosines hyperbolic function sech, see for instance Pétri & Kirk (2007). We thus adopt the following expression for the density

$$K_e(\vec{r}, t) = \frac{(N - N_0) \, \mathrm{sech}^2(\Delta_\varphi \, \psi) + N_0}{r^2} \tag{2.4}$$

N_0 sets the minimum density in the stripes, between the current sheets, whereas N defines the highest density inside the sheets. However, in order to allow different peak intensities in the light curves, we choose different maximum densities in two consecutive sheets, namely N_1 and N_2. The radial motion of the wind at a fixed speed imposes an overall $1/r^2$ dependence on this quantity, due to conservation of particle number. However, adiabatic losses in the current sheets due to pressure work will cool down this distribution function in such a way that K_e decreases with an additional factor $1/r^{2/3(p+2)}$, see Kirk (1994). As already done in a previous work, we assume the emission commences when the wind crosses the surface defined by $r = r_0 \gg r_{\rm L}$. Let us now discuss the exact form of the emissivity functions in the striped wind for the inverse Compton radiation.

2.3 Inverse Compton emissivity

We assume an isotropic distribution of mono-energetic target photons ε with density $n_\gamma(\varepsilon)$ in the observer frame. The total emissivity is denoted by $j_{\rm ic}^{\rm obs}$. Knowing the inverse Compton emissivity, the light curves are obtained by integration over the whole wind region. This wind is assumed to extend from a radius r_0 to an outer radius $r_{\rm s}$ which can be interpreted as the location of the termination shock. Therefore, the inverse Compton radiation at a fixed observer time t is given by

$$I_{\rm ic}^{\rm obs}(t) = \int_{r_0}^{r_{\rm s}} \int_0^\pi \int_0^{2\pi} j_{\rm ic}^{\rm obs}(\vec{r}, t_{\rm ret}) \, r^2 \sin\theta dr d\theta d\varphi \tag{2.5}$$

The retarded time is expressed as $t_{\rm ret} = t - \|\vec{R}_0 - \vec{r}\|/c \approx t - R_0/c + \vec{n} \cdot \vec{r}/c$. The approximation is valid if the observer, located at $\vec{R}_0$, is very far away from the radiating system, $R_0 \gg r_{\rm s}$. Eq.(2.5) is integrated numerically. We compute the

inverse Compton intensity for several frequencies from far below the low cut-off frequency to far over the high frequency cut-off. We are therefore able to predict the phase resolved spectral variability and the pulse shape simultaneously. The results and applications to some γ-ray pulsars are discussed in the next section.

3 APPLICATION TO γ-RAY PULSARS

We apply the aforementioned model to inverse Compton scattering of low-energy photons from the cosmic microwave background with typical energy of $\varepsilon_{\rm cmb} = k_B\, T_{\rm cmb} = 2.36 \times 10^{-4}$ eV and energy density of 2.65×10^5 eV/m^3. We focus on 2 pulsars, namely, Vela and Geminga.

3.1 Geminga pulsar

In our best fit, we choose an inclination of the magnetic moment with respect to the rotation axis of $\chi = 60^o$. In order to obtain a phase separation of 0.5 between the two pulses, we have to adopt an inclination of the line of sight $\zeta = 90^o$. The Lorentz factor of the wind is $\Gamma = 10$.

Results for the light-curve above 100 MeV and the definition of the different phase intervals is shown in Fig. 1. The rising and falling shape of both pulses are well fitted by our model. The corresponding spectra are shown in Fig. 2. The spectral variability is reproduced with satisfactory accuracy except for the OP phase for which the intensity is overestimated.

3.2 Vela pulsar

In our best fit, we choose an inclination of the magnetic moment with respect to the rotation axis of $\chi = 60^o$ and an inclination of the line of sight $\zeta = 76^o$. The Lorentz factor of the wind is $\Gamma = 16$.

Results for the light-curve above 100 MeV and the definition of the different phase intervals is shown in Fig. 1. The corresponding spectra are shown in Fig. 2. The spectra within the two pulses, P1/2, IP1, LW2 and TW1 are well reproduced as well as the cut off energy around a few GeV. The other phases still need some intensity level readjustment.

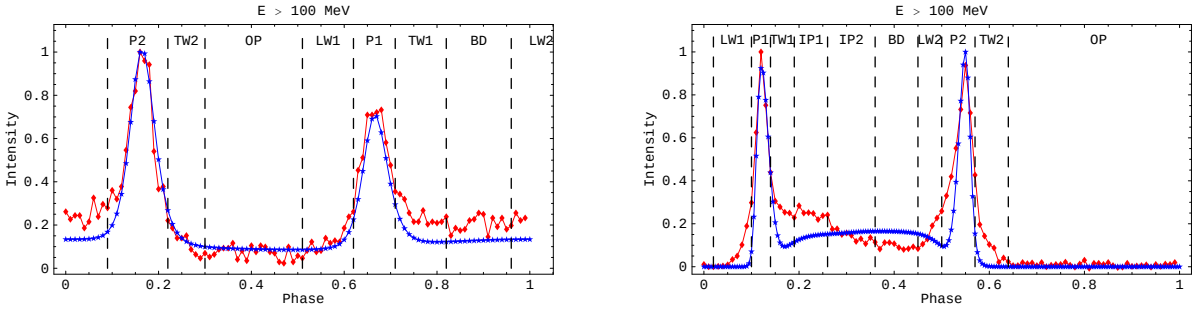

Fig. 1. Gamma-ray light curve above 100 MeV of Geminga, on the left and Vela, on the right, fitted with the inverse Compton emission from the striped wind.

4 CONCLUSION

In the striped wind model, the pulsed high-energy emission from pulsars arises from regions well outside the light-cylinder. By computing the inverse Compton emission on the CMB photons, we were able to fit the EGRET data of the light-curves and spectra for several gamma-ray pulsars such as Vela and Geminga.

References

Bogovalov, S. V. 1999, A&A, 349, 1017

Coroniti, F. V. 1990, ApJ, 349, 538

Fierro, J. M., Michelson, P. F., Nolan, P. L., & Thompson, D. J. 1998, ApJ, 494, 734

Kirk, J. G. 1994, in Saas-Fee Advanced Course 24: Plasma Astrophysics, ed. A. O. Benz & T. J.-L. Courvoisier, 225

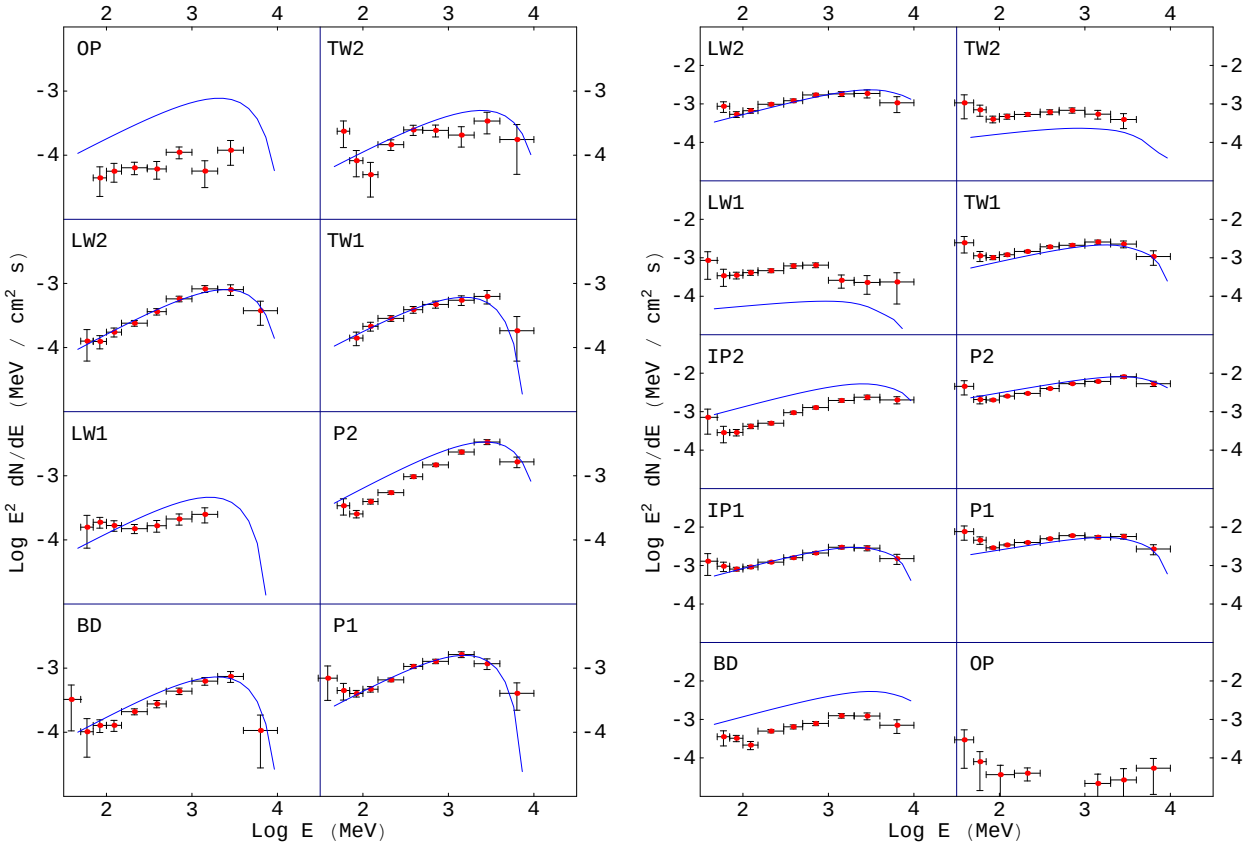

Fig. 2. Phase-resolved inverse Compton emission from the Geminga pulsar, on the left and the Vela pulsar, on the right, for different phase intervals: bridge (BD), off-pulse (OP), interpulse 1/2 (IP1/IP2), leading wing 1/2 (LW1/LW2), peak 1/2 (P1/P2), trailing wing 1/2 (TW1/TW2), for the definition of the intervals see Fierro et al. (1998).

Kirk, J. G., Skjæraasen, O., & Gallant, Y. A. 2002, A&A, 388, L29

Michel, F. C. 1994, ApJ, 431, 397

Pétri, J. & Kirk, J. G. 2005, ApJL, 627, L37

Pétri, J. & Kirk, J. G. 2007, Plasma Physics and Controlled Fusion, 49, 1885